Light Scattering Study of Highly Absorptive, Non-fractal, Hematite Aggregates

Prakash Gautam[a], Justin B. Maughan[a], Jan Ilavsky[b] and Christopher M. Sorensen[a]*

[a]Department of Physics, Kansas State University, Manhattan, KS 66506, USA
[b]Advanced Photon Source, Argonne National Laboratory, Lemont, IL 60439, USA

*Corresponding author. E-mail address: sor@phys.ksu.edu (C.M. Sorensen).

Highlights:
- The scattered light was enhanced in the backscattering regime despite large imaginary refractive index.
- Enhancement backscattering for the aggregate is due to internal multiple scattering between the grains within the aggregate.
- Bimodal size distribution causes an extended Guinier regime.
- Highly refractive particles displays two-dimensional diffraction properties.

Abstract

We present measurements of the scattered light intensity by aerosolized hematite aggregate particles. The measurements were made at a wavelength of 532 nm in the scattering angle range from 0.32° to 157°. Hematite has high values of the real and imaginary parts of the refractive index $m = n + i\kappa = 3 + i0.5$ at the studied wavelength. Scanning electron micrographs (SEM) indicated that the particles were aggregates whereas the optical microscope pictures showed that the aerosol had a bimodal distribution with effective mean diameters of roughly 1 and 10 μm. This is consistent with the light scattering results which displayed two Guinier regimes. The aggregates were composed of smaller grains with an approximate size of 200 nm. Ultra Small-Angle X-ray Scattering (USAXS) indicate that the aggregates were uniform and non-fractal. Mie calculations for a sphere equivalent to the aggregate size were compared to the experimentally observed results. The observed results showed an enhanced backscattering, whereas the Mie calculations did not due to the large imaginary part of the refractive index. Hematite aggregates were simulated by assuming they were composed of spherical monomers inside a spherical volume. Then the light scattering was calculated using the T-matrix method for these simulated aggregates. The calculated results show an enhanced backscattering. We present a dimensional analysis to estimate the extent of multiple scattering within the aggregate and find a correlation between the average number of scattering events within the aggregate and the enhancement in the backscattering.

1. Introduction

A coherent description and understanding of light scattering by spherical particles is well understood [1–3]. Many naturally occurring aerosol particles are highly irregular in shape and scattering by such irregular particles is a problem of current interest. A large fraction of the

aerosols by mass in the Earth's atmosphere is made up of minerals dust, volcanic ash, desert dust and soot particles that are highly irregular in shape. The way in which they scatter and absorb light plays an important role in climate forcing and climate models. Iron oxide constitutes an important component of mineral dust particles and these minerals are strong absorbers at visible wavelengths. For example, hematite comprises up to 1% of Saharan dust and up to 2.6% of Icelandic dust by mass [4–8].

In this article we present light scattering due to hematite particles. Hematite (α-Fe_2O_3), an iron oxide mineral, is found in both the Earth and the Martian atmospheres. Hematite has a large absorption cross-section in comparison to other mineral aerosols [4,9]. Hematite is believed to be the main component that gives Mars its orange color [9–11].

We study the angular distribution of the light scattering intensity from hematite particles. This paper is focused especially on the backscatter region. The backscattering region is more sensitive to particle shape irregularities and heterogeneities than forward scattering region [3]. In this paper we apply Q-space analysis [12–15] for the experimentally observed scattered light. In Q-space analysis the scattered intensity is plotted versus the magnitude of the scattering wave vector q on a log-log scale. The scattering wave vector is the fundamental variable in the Q-space analysis, and its magnitude is given by

$$q = 2\,k\,\sin(\theta/2), \tag{1}$$

where $k = 2\pi/\lambda$, λ the optical wavelength and θ is the scattering angle. Guinier analysis of the Q-space plot estimates the particle sizes of the scatterer.

Scanning electron microscope images and Ultra Small-angle X-ray Scattering (USAXS) data show that hematite particles are uniform, non-fractal aggregates. Hematite is known to have large real and imaginary parts of the refractive index [4,16,17]. Whereas a large imaginary refractive index typically quenches enhanced backscattering, our experimental data show enhanced backscattering. We present an argument that this occurs due to internal cluster multiple scattering between the monomer grains of the aggregate.

2. Experimental Method

2.1 Optical setup

For our experiments we used a setup very similar to that described in [18]. The incident laser beam used was polarized perpendicular to the scattering plane. It had a wavelength $\lambda = 532$ nm and a beam waist of 0.7 mm. Two sixteen channel detector arrays observed light in the forward and side angle directions. The forward scattering setup was based on a design by Ferri [19]. The scattering volume was a cylinder with a diameter of 0.7 mm and a length of 3 mm where the horizontal laser beam interacted with the vertically flowing aerosol stream coming from a 3 mm inner diameter brass tube. The forward detector was calibrated by diffracting the laser beam through a 10 μm single slit placed at the scattering volume. The forward detector collected the scattered light at 16 angles from 0.3° to 9.89°. Detection at small angles is very important for characterizing large size particles.

For the side scattering a custom elliptical mirror was used to collect the scattered light. The scattering volume was located at the near focal point of the elliptical mirror and a 1 mm circular aperture iris was located at the far focal point of the elliptical mirror. The scattered light coming through the iris was collimated by a collimating lens and was measured by the side detector. For the alignment of the side detector, we placed 1 mm × 3 mm capillary tube where the scattering volume is located. We filled the capillary tube with a glowing agent to make sure that 15 channels of the detector received the same intensity. The 16th channel was sacrificed as a monitor. The 15 side scattering angles ranged from 15° to 157°. Thus, our apparatus covers a wide range of scattering angles from 0.3° to 157°. This corresponds to a q range of 660 cm^{-1} to 2.3×10^5 cm^{-1}.

To calibrate forward scattering with side scattering detectors, we used two mirrors in such a way that the initial direction of the incident laser beam was offset by 6°. Thus, the side scattering angle was offset by that much to transform the 15° angle to 9° on the side scattering detector which then lies in the forward detector range. This yields a multiplication factor, to connect forward and side scattering. The two detectors are connected to data acquisition device and to the computer. To aerosolize the hematite particles, we used a lab-made dust generator.

2.2 Sample Characterization

The hematite sample (α-Fe_2O_3) investigated in this study was obtained from US Research Nano-Materials Inc. Scanning Electron Microscope (SEM) and optical microscope images of the hematite sample are given in Fig. 1. SEM shows the hematite sample is bimodal with aggregates as large as 10 μm. The aggregates are composed of small grains, monomers, that look like rounded polyhedrons with a mean diameter of 2a $\simeq$ 200 nm. The optical microscope pictures in Fig. 1d was created by blowing the hematite into a 17L chamber in a manner very similar to that which blows the particles through the optical scattering volume. The aerosol was allowed to settle with time onto microscope slides at the bottom of the chamber. Thus this picture represents the light scattering aerosol, and that aerosol is seen to be bimodal with mode sizes (rough diameters) of approximately 1 and 10 μm dominated in number by the smaller size.
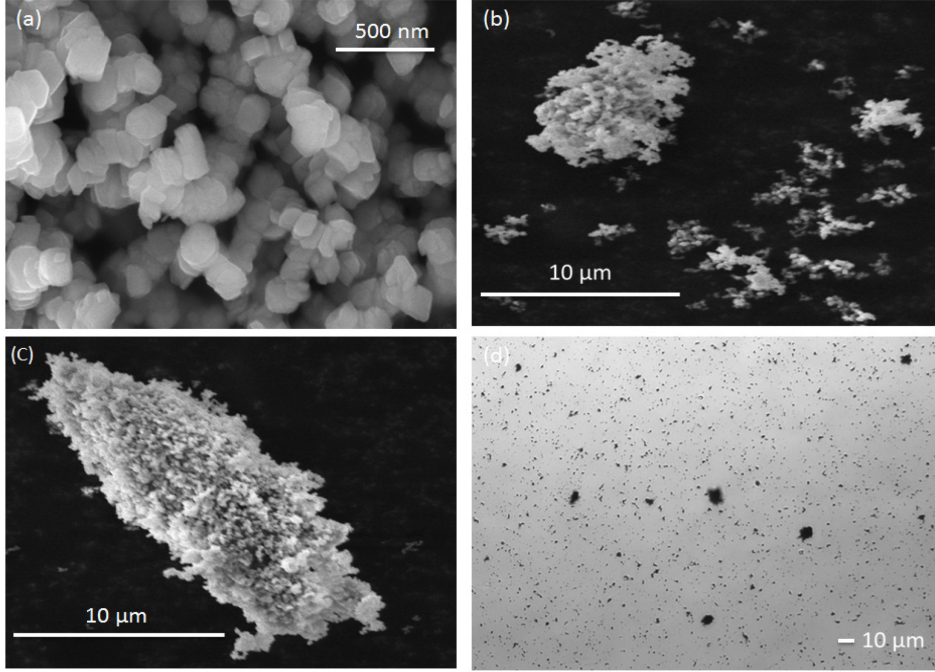
Figure 1. The images of hematite (Fe_2O_3) particles: (a), (b) and (c) under a scanning electron microscope (SEM) and (d) under an optical microscope.

The SEM pictures show that the larger hematite particles are aggregated in nature, but to identify the nature of aggregates, we performed Ultra Small-Angle X-ray Scattering (USAXS) to determine the structure factor S(q) of the particles [20]. The result displayed in Fig. 2 shows two Porod regimes with slope -4 to indicate power laws $S(q) \sim q^{-4}$. Most generally, the magnitude of the Porod exponent is $D_p = 2D_m - D_s$ [21], where D_m and D_s are the mass and surface scaling dimensions, respectively. These exponents describe the power law scaling of an object's mass with an overall linear size like the mean radius. A value of $D_p = 4$ implies (not uniquely) $D_m = 3$ and $D_s = 2$ to indicate non-fractal, "three dimensional", objects.

To model the USAXS result and thereby gain more insight for the structure of the aggregates, we used a variation of the Eden growth model to create aggregates [22]. Three model aggregates were grown into spherical volumes of radii 8, 10, and 12 µm with a monomer size of radius a =100 nm until a volume fraction of 0.3 was reached. This volume fraction was determined by massing the real sample with and without a penetrating liquid medium. The model aggregates were discretized and placed onto a cubic lattice with point spacing of 20 nm. To compare with the USAXS data the real space coordinates of the model aggregates were Fourier transformed into the reciprocal q-space. The scattered intensity is proportional to the square of the Fourier transformed real space coordinates, which is the structure factor, and for a discretized system it is given by [23]

$$S(\vec{q}) = \sum_{l,j}^{N} e^{i\vec{q}\cdot(\vec{r}_l - \vec{r}_j)} \tag{2}$$

where $\vec{r}_l$ and $\vec{r}_j$ are the position vectors of the lth and jth points within the aggregate, respectively, and N is the number of points that the aggregate has been discretized into.

The average of the structure factors for the spherical volumes of radii 8, 10, and 12 μm is shown in Fig. 2. The average structure factor is used to minimize the diffraction ripple structure. In Fig. 2 it can be seen that the calculated structure factor and USAXS data agree very well at small q, which corresponds to the length scales of the aggregates, until inverse q (which is a length) becomes comparable with the monomer size. The disagreement at larger q comes about due to the use of a single monomer size. The use of a single sized monomer yields a form factor for the monomer with a ripple structure. Nevertheless, the envelope of the form factor at large q shows a slope of -4 consistent with the USAXS data. Given the fairly uniform morphology of the aggregates seen in Fig. 1, the USAXS data and our successful modeling of the data, we conclude that the hematite aggregates are not fractal and have mass and surface scaling dimension of $D_m = 3$ and $D_s = 2$, respectively.
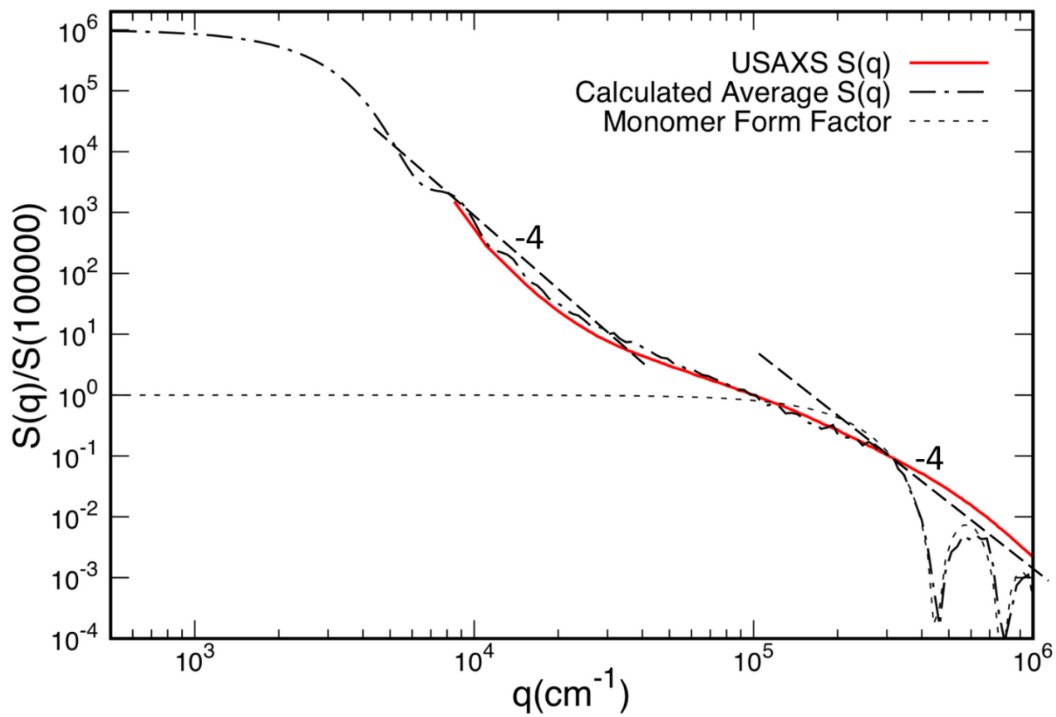

Figure 2. Ultra Small-Angle X-ray Scattering (USAXS) data, solid red line, for the structure factor S(q) of the hematite. Power laws of q^{-4} at large and small q values indicate that the primary (monomers) and aggregated particles, respectively, have mass scaling dimension $D_m = 3$ and surface scaling dimension $D_s = 2$. This implies a non-fractal nature of both the aggregates and, not surprisingly, the monomers.

To conclude our sample characterization it is known that hematite is a birefringent material. The real and imaginary values of the refractive index for the extraordinary ray is n = 2.8

and $\kappa = 0.5$ and for the ordinary ray is $n = 3.2$ and $\kappa = 0.5$, respectively, for $\lambda = 532$ nm [4] which is based on the previous work by [24]. In our calculations, we used the refractive index $m = n + i\kappa$ = $3 + i0.5$, the average values of extraordinary and ordinary rays, weighted equally [9,25].

3. Results

The experimental scattered intensity plotted versus q on a double logarithmic scale, Q-space analysis, is shown in Fig. 3a. This is normalized to 1 at the smallest measuring angle of 0.3° ("forward normalized"). Three notable features are observed: 1) an extended Guinier regime in the range 10^3 cm^{-1} < q < 10^4 cm^{-1} with two Guinier crossovers 2) a short power law regime with exponent -3, and 3) enhanced backscattering at large q corresponding to angles of θ = 129°, 139°, 149° and 157°. It is this backscattering feature that is the major subject of this paper. Figure 3b shows the same data plotted versus linear scattering angle θ, the conventional manner. A non-descript curve results unable to resolve the two Guinier regimes and the power law.
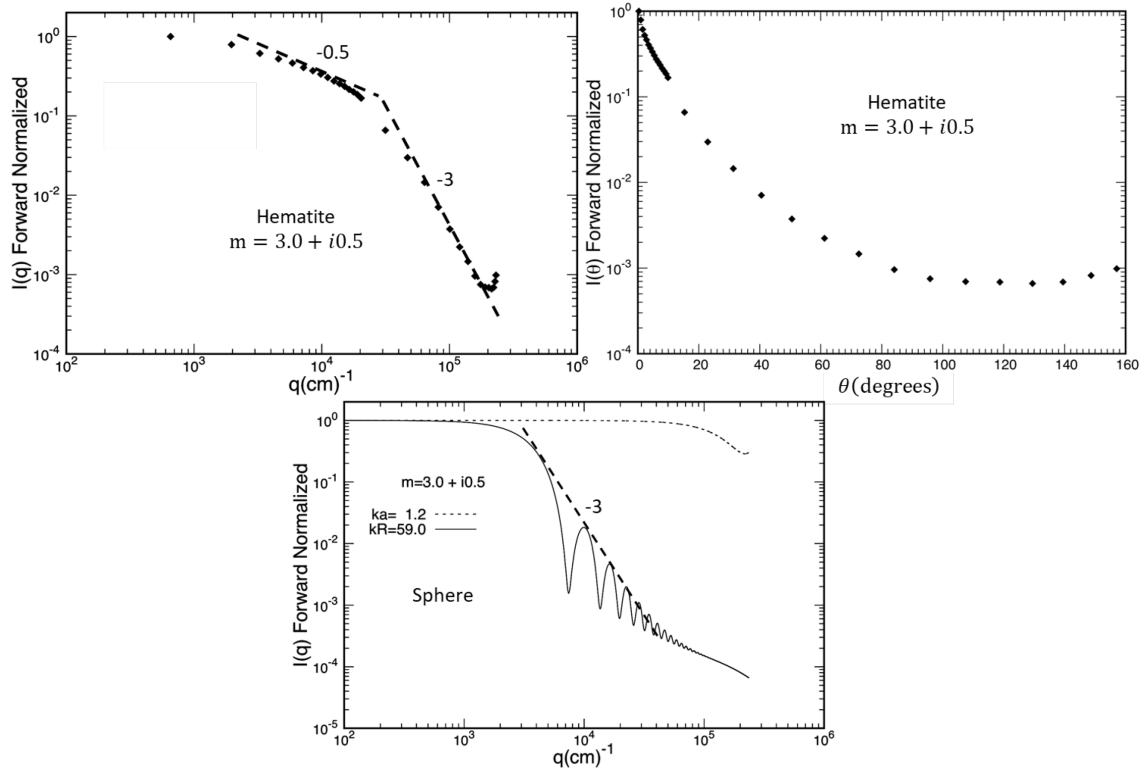

Figure 3. (a) Forward normalized scattered intensity data versus q plotted double logarithmically (Q-space analysis) of the light scattered intensity of the hematite aggregate particles observed experimentally, (b) same data plotted versus linear scattering angle θ, and (c) Forward normalized Mie scattered intensity for a sphere with a radius R = 1.2 μm similar to the hematite aggregate particles, solid line, and spherical hematite grains of radius a = 100 nm, dashed line. Sphere size parameters, kR and ka, are given. Dashed lines indicate power laws with slope designated.

An explanation of the first feature lies with the bimodal size distribution seen in Figs.1b and d. Q-space analysis facilitates the determination of the size of any shape of particles via Guinier analysis [26,27]. For our purposes here, a complete Guinier analysis is not necessary. Instead we will use the fact that Guinier regime is an inflection of the slope of I(q) versus q when plotted double logarithmically, typically at small q to imply a length scale equal to the inverse of the q value at the crossover. The data in Fig. 3(a) suggest two inflections due to two length scales [28]. The first inflection is at $q \simeq 10^3$ cm^{-1} to imply length scale of $q^{-1} \simeq 10$ μm and the second inflection is at $q \simeq 10^4$ cm^{-1} to imply a length scale of $q^{-1} \simeq 1$ μm. These semi-quantitative length scales are consistent with the bimodality depicted in Figs.1b and d. Note that this bimodality is essentially impossible to see in the data when been plotted versus linear scattering angle, Fig. 3b.

An explanation of the second features, the brief power law, lies with the large refractive index of hematite. We have shown that for spheres with large real and imaginary parts to the refractive index the scattering limits to a Fraunhofer diffraction pattern for a circular aperture or, by Babinet's principle, circular obstacle [29]. This is particularly true when the product of the imaginary refractive index and the size parameter, κkR, is large. The parameter κkR [30] is the ratio of the particle radius to the optical penetration depth, such that when $\kappa kR \geq 3$, the incident light barely penetrates the object so that a particle acts like an opaque object. Ignoring the ripples, all diffraction patterns have a constant scattered intensity at small q followed by a crossover Guinier regime, and then at largest q, a power law Porod regime, which is an envelope for the ripples with q^{-Dp} functionality. A Porod exponent of $D_p = 3$ results for any shape with mass and surface scaling dimensions or $D_m = 2$ and $D_s = 1$, respectively (recall from above $D_p = 2D_m - D_s$). The fact that the hematite aggregates have mass and surface scaling dimensions of $D_m = 3$ and $D_s = 2$, respectively, means that their projections will have $D_m = 2$ and $D_s = 1$, so that their diffraction patterns will have Porod exponents of $D_p = 3$. This explains the observed power law.

Given all this, we calculated circular aperture diffraction patterns for radii of 1 and 10 μm and averaged them over a minor size distribution to eliminate the ripple structure. We added these together and adjusted the relative intensities to yield a power law of slope -0.5 between the two Guinier regimes, as seen in the data, Fig. 3a. The results are shown in Fig. 4 and are seen to replicate the data in Fig. 3a, except for the enhanced backscattering. Given that the scattering in this regime of size and refractive index is proportional to the diameter to the fourth power, the implication is that there are 10^4 more small particles than big ones. This is consistent with Fig. 1d.
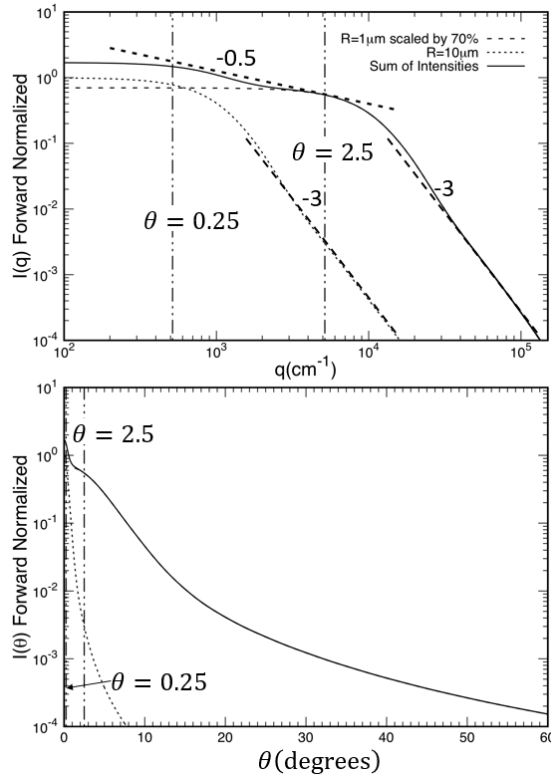
Figure 4. Forward normalized circular aperture diffraction pattern envelopes for radii of 1 μm and 10 μm. Top: versus q plotted double logarithmically (Q-space analysis); Bottom: versus the scattering angle θ. Both plots indicate scattering angles of 0.25° and 2.5° with vertical dash-double-dot lines. The two individual Q-space analysis plots for R = 1 μm and 10 μm show a single inflexion at the Guinier regime, a power law envelope of q^{-3} with no enhanced backscattering. The sum of intensities for these two plots shows an extended Guinier regime with slope -0.5 followed by a power law envelope of q^{-3}. Note that these features are not apparent in the normal plotting of scattered intensity versus linear scattering angle.

It is interesting to compare this conclusion to the USAXS analysis. In the USAXS analysis the large size mode of the bimodal size distribution with radii on the order of R ≃ 10 μm dominated the X-ray scattering. In the analysis of the light scattering in Fig. 4 the small size mode of the bimodal size distribution with radii on the order of 1 μm dominated the light scattering. The difference lies in the fact that the refractive index for X-rays is nearly unity with no imaginary part. Then the scattering lies in the Rayleigh-Debye-Gans limit where the forward scattering is proportional to R^6. On the other hand, large refractive particles, like our hematite, are in a regime of scattering for which the forward scattering is proportional to R^4. This difference in size functionality applied to our particular bimodal size distribution shifts the dominance of one mode over the other between the two sets of data.

The rest of this paper considers the third feature, the enhanced backscattering at large q. Our light scattering results are compared to the results of Mie calculation for a sphere with the same perimeter radius of the hematite particles in Fig.3c. For the Mie calculations, we took R =

1.2 μm, the approximate size for aggregate hematite particles inferred from microscopy measurements. This radius corresponds to a size parameter of $kR = 2\pi R/\lambda = 14.2$. The size parameter of the grain is $ka = 1.2$, where $a = 100$ nm. Figure 3c shows that the hematite size equivalent sphere has no enhanced backscattering, while the single grain does. This can be explained with the parameter κkR [15,30], which for the sphere is $\kappa kR = 7.1$, a very large value, such that enhanced backscattering is not observed. On the other hand, for the grain $\kappa ka = 0.6$ which is small enough to allow for enhanced backscattering, and indeed, the Mie calculation in Fig. 3c indicates that this is true. However, the data in Fig. 3a indicate that hematite aggregates with the same size as the sphere show enhanced backscattering. Accordingly, we can speculate that the backscattering of the aggregate is either due to the grains in the aggregate particles or the aggregate structure.

4. Theoretical Calculations

Investigations of backscattering phenomena by aggregates are "neither few nor small", e.g. [31–37]. These studies are mostly theoretical, and essentially all see enhanced backscattering beyond scattering angles of ca. 140°, as do we with hematite. However, these previous studies are oriented towards astrophysical situations such as lunar and planetary regoliths, cometary dusts, etc. Hence the refractive indices are significantly smaller than that of hematite. Given this, we have performed our own theoretical calculations directly relevant to our experimental work.

To study the effects of the hematite aggregate structure on the light scattering we simulated the hematite aggregates with the variant Eden growth model aggregates described above to fit the USAXS data. An example is shown in Fig. 5. Then the light scattering was calculated using the T-matrix method [38]. Given the size information in Fig. 1, our Guinier analysis in Fig. 4 and consideration of computational time constraints, we studied a spherical volume of radius $R = 1.2$ μm. The monomers were spherical with radii of $a = 100$ nm, which is equivalent to the size of the hematite grains. The number of monomers inside the diameter 2.4 μm spherical volume was varied from $N = 30$ to $N = 692$, thereby yielding particle volume fractions from $f_v = 0.017$ to $f_v = 0.40$. The light wavelength used was $\lambda = 532$nm. The incident light was linearly polarized perpendicular to the scattering plane. Figure 6 shows the results of these calculations for a monomer refractive index of $m = 3 + i0.0$, Fig. 7 shows results for a monomer refractive index of $m = 3 + i0.5$, which is the refractive index of hematite at $\lambda = 532$nm, and Fig. 8 shows results for $m = 3 + i1.0$.
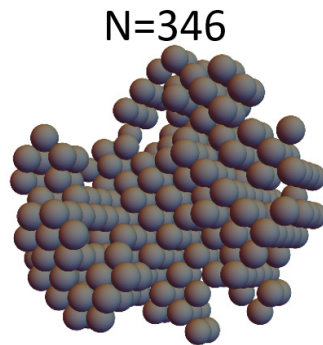

Figure 5. An example of the variant Eden growth model aggregates used for the T-matrix calculations.
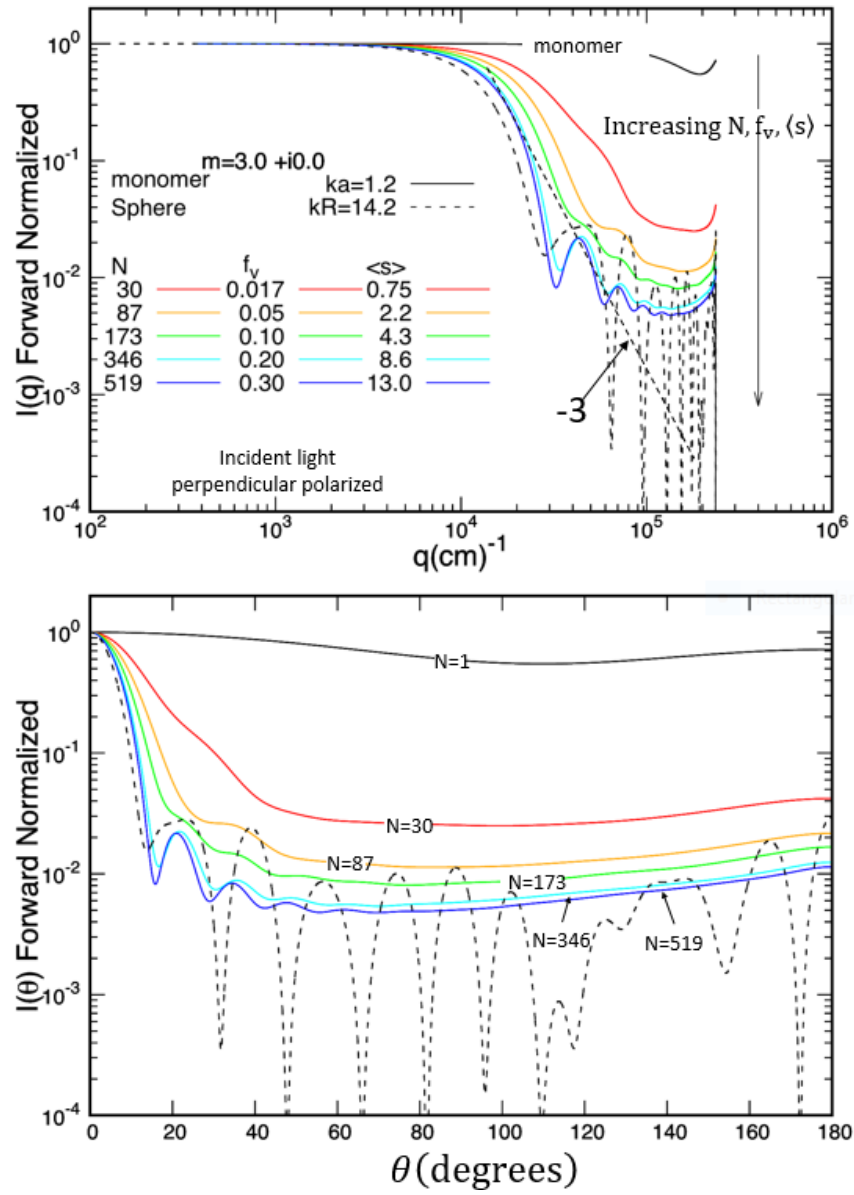
Figure 6. Calculated forward normalized scattered intensity for an aggregate formed as a spherical volume with a diameter of 2.4 μm with N randomly distributed spherical monomers of diameter 2a = 200 nm within. Top: versus q plotted double logarithmically (Q-space analysis); Bottom: versus the scattering angle θ. The corresponding monomer particle volume fractions are denoted by f_v. The monomers have a refractive index of m = 3 + i0.0. The light wavelength is λ = 532nm linearly polarized perpendicular to the scattering plane. The average number of scattering events with in the aggregate volume is <s>, see Eq. (4), below. Also shown is the scattering for a single monomer and for a solid sphere with diameter D = 2.4 μm. Dashed line indicates a slope of -3.
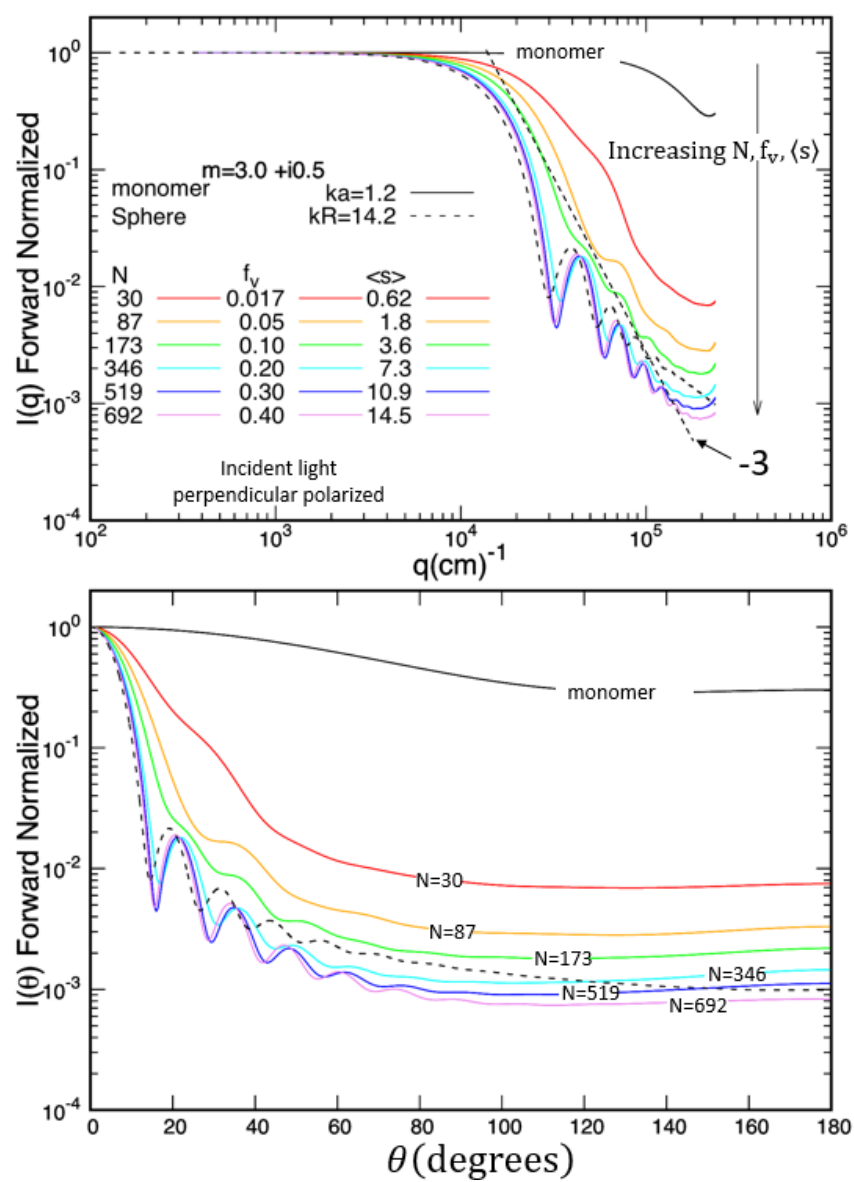
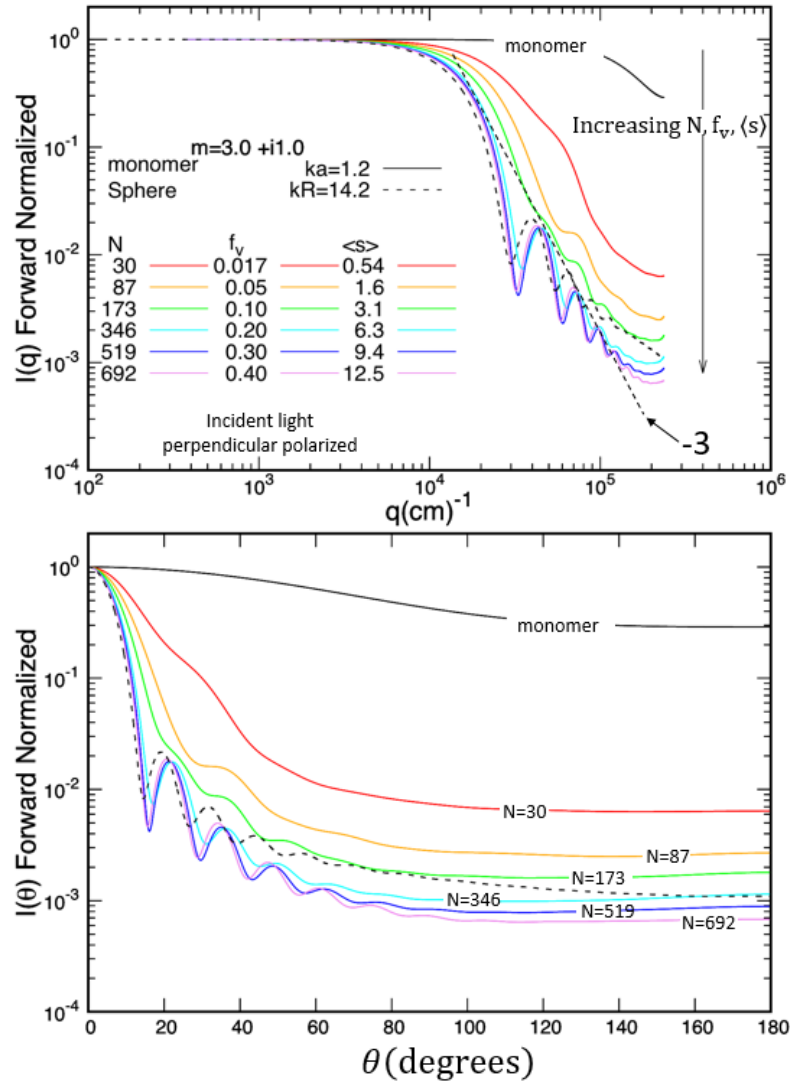Figure 7. Same as Fig. 6 except m = 3 + i0.5, the refractive index of hematite.

Figure 8. Same as Figs. 6 and 7 except m = 3 + i1.0.

The systematic study displayed in Figs. 6 to 8 used two variables: 1) a wide range of monomer volume fractions inside the spherical volume to explore the effect of the aggregate structure and 2) the grain refractive index imaginary part varied as $\kappa = 0.0$, 0.5 to 1.0. This change led the parameter κka of the grain to range from 0.0 to 0.6 and to 1.2 and yielded significant, moderate and no enhanced backscattering by the monomer grain respectively, see Figs. 5 to 7.

Figure 6 uses m = 3 + i0.0. The monomer, the same size solid sphere and the aggregates all show enhanced backscattering. Figure 7 for m = 3 + i0.5 shows modest enhanced backscattering for the monomer, no enhanced backscattering for the solid sphere and enhanced backscattering for the aggregate. Figure 8 uses m = 3 + i1.0 to find no enhanced backscattering for the monomer, no enhanced backscattering for the solid sphere and enhanced backscattering for the aggregate. Thus while the imaginary part of the refractive index quenched the enhanced backscattering in the monomer and the same sized sphere, the enhanced backscattering remained in the aggregates. We

conclude that the enhanced backscattering from the aggregate is due to the aggregate structure. This is a direct result of Maxwell's equations which are the foundation of the computational method used.

Close inspection of Figs. 6 to 8 shows that larger imaginary part κ does cause smaller enhanced backscattering for the aggregates. This could be augmentation of the aggregate based backscattering with the monomer backscattering of lack of it. One also observes that the enhanced backscattering initially increases with the number of monomers N. The enhancement levels off around the particle volume fractions $f_v = 0.20$ to $f_v = 0.30$, and then declines when the particle volume fraction reaches $f_v = 0.40$. This decline suggests that the spherical volume starts to behave as homogenous [38]. Our overall conclusion is that the aggregate's enhanced backscattering occurs even when the individual grains have none. This implies that the enhanced backscattering is a colligative effect related to the aggregate structure.

We now hypothesize a physical interpretation for the enhanced backscattering in the aggregate as due to multiple scattering between the monomer grains. Our approach will use a dimensional analysis to estimate the extent of multiple scattering within the hematite aggregates.

Inter-grain multiple scattering within the aggregate will depend upon the grain scattering cross section, with dimension length squared, and the number density of the grains, with dimension of inverse length cubed. Thus a length scale can be formed from these two quantities as the inverse of their product. It is reasonable to claim that this length scale is related to the mean free path (mfp) of the light wave between scattering events [39]. Thus we write

$$mfp = \frac{1}{n\, C_{sca,mon}} = \frac{4\pi a^3}{3 C_{sca,mon} \cdot f_v} \qquad (3)$$

where, $C_{sca,mon}$ is the total scattering cross-section of a monomer grain, n is the number density of the monomers, f_v is the monomer volume fraction, and a is the monomer radius.

This scattering length scale can be compare to the length scale of the entire aggregate to get a dimensionless number that is related to extent of the multiple scattering which would be the average number of scattering events <s>

$$<s> = \frac{R}{mfp} \qquad (4)$$

To continue we expect the intra-aggregate scattering to be stochastic and governed by the Poisson distribution. Then the probability of s scattering events within the aggregate is

$$P(s) = \frac{<s>^s}{s!} e^{-<s>} \qquad (5)$$

Multiple scattering plays a significant role for non-absorptive particles when the average number of scattering events <s> becomes large.

We now test the descriptive ability of our hypothesis that enhanced backscattering from the aggregate is due to multiple scattering between the monomer grains by seeing if our definition of the average number of scattering events <s> is correlated to the enhanced backscattering.

We have calculated the average number of scattering events <s> for the spherical scattering volume of diameter 2.4 μm. The enhancement in the backscattering for different volume fractions was quantified by calculating the ratio of scattered intensity at 157°, our largest

experimental angle, to the minimum intensity near 129° i.e. (I (157°)/I (Min)). This ratio is plotted versus the average number of scattering events <s> and volume fractions f_v in Fig. 9.
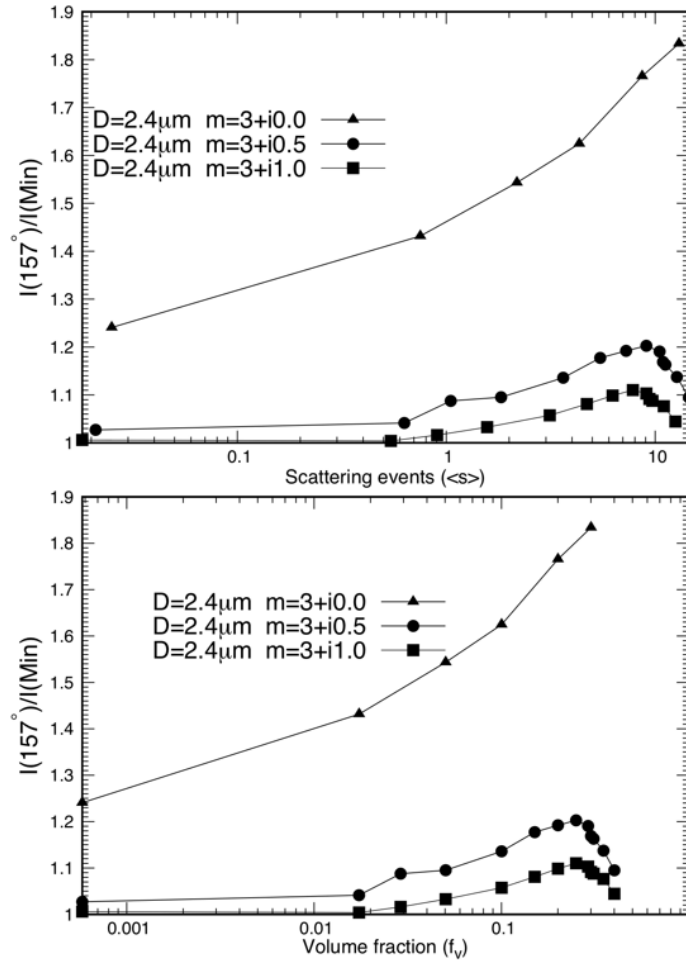

Figure 9. Plot showing the enhancement in the backscattering, the ratio I(157°)/I(Min), versus (top) the average number of scattering events <s> in the aggregate, and (bottom) the volume fraction f_v of monomers in the aggregate.

Figure 9 (top) shows that when the average number of scattering events in the aggregate is very small, there is very little enhanced backscattering. With increasing scattering events, there is an increase in the backscattering enhancement and this enhancement peaks around <s> ≏ 9. When $\kappa \geq 0.5$, further increase in the scattering events led the backscattering enhancement to decrease, see Fig. 9 (bottom). The behavior for m = 3 + i0.0 shows no peak, but the computation was limited by computational time constraints such that volume fractions where the other two refractive indices showed a peak where not obtained when $\kappa = 0$. The decrease might occur because with increasing number of monomers, the spherical volume starts to act like a homogenous particle, which we have seen has no enhanced backscattering for the values of κkR that we are considering. Nevertheless, our tentative multiple scattering hypothesis correlates the increase and the ultimate decrease in the enhanced backscattering with increasing monomer volume fraction.

5. Conclusion

We have studied the light scattering due to densely aggregated hematite particles composed of monomer grains. Hematite is a naturally occurring mineral with a large refractive index of m = 3.0 + i0.5 at λ = 532 nm, the wavelength used in our study. USAXS measurement showed that the aggregates were not fractal. Light scattering Q-space analysis uncovered a bimodal size distribution consistent with microscopy. Enhanced backscattering was observed for angles greater than 130°. It was shown with model calculations, that this enhanced backscattering was due to the aggregate structure despite the large imaginary part of the refractive index which quenched enhanced backscattering for the aggregate monomers and aggregate size equivalent sphere. It was proposed that aggregate internal multiple scattering between monomers within the aggregate was the cause of the enhanced backscattering. A dimensional analysis for the average number of internal scattering events supported that proposition.

References

[1] van de Hulst HC. Light Scattering by Small Particles, Reprint, edition, Dover Publ., New York. 1981.
[2] Bohren CF, Huffman DR. Absorption and scattering of light by small particles. John Wiley & Sons; 2008.
[3] Mishchenko MI, Travis LD, Lacis AA. Scattering, absorption, and emission of light by small particles. Scattering, Absorption and Emission of Light by Small Particles /Michael I Mishchenko, Larry D Travis, Andrew A Lacis Cambridge, UK : Cambridge University Press, 2002.
[4] Sokolik IN, Toon OB. Incorporation of mineralogical composition into models of the radiative properties of mineral aerosol from UV to IR wavelengths. J Geophys Res 1999;104:9423–44. https://doi.org/10.1029/1998JD200048.
[5] Veghte DP, Moore JE, Jensen L, Freedman MA. Influence of shape on the optical properties of hematite aerosol. Journal of Geophysical Research: Atmospheres 2015;120:7025–39. https://doi.org/10.1002/2015JD023160.
[6] Zhang XL, Wu GJ, Zhang CL, Xu TL, Zhou QQ. What is the real role of iron oxides in the optical properties of dust aerosols? Atmos Chem Phys 2015;15:12159–77. https://doi.org/10.5194/acp-15-12159-2015.
[7] Kandler K, SchüTZ L, Deutscher C, Ebert M, Hofmann H, JäCKEL S, et al. Size distribution, mass concentration, chemical and mineralogical composition and derived optical parameters of the boundary layer aerosol at Tinfou, Morocco, during SAMUM 2006. Tellus B: Chemical and Physical Meteorology 2009;61:32–50. https://doi.org/10.1111/j.1600-0889.2008.00385.x.

[8]   Prospero JM, Bullard JE, Hodgkins R. High-Latitude Dust Over the North Atlantic: Inputs from Icelandic Proglacial Dust Storms. Science 2012;335:1078–82. https://doi.org/10.1126/science.1217447.

[9]   Muñoz O, Volten H, Hovenier JW, Min M, Shkuratov YG, Jalava JP, et al. Experimental and computational study of light scattering by irregular particles with extreme refractive indices: hematite and rutile. A&A 2006;446:525–35. https://doi.org/10.1051/0004-6361:20053727.

[10]   Banin A, Ben-Shlomo T, Margulies L, Blake DF, Mancinelli RL, Gehring AU. The nanophase iron mineral(s) in Mars soil. J Geophys Res 1993;98:20831. https://doi.org/10.1029/93JE02500.

[11]   Morris RV, Lauer HV. Matrix effects for reflectivity spectra of dispersed nanophase (superparamagnetic) hematite with application to Martian spectral data. J Geophys Res 1990;95:5101. https://doi.org/10.1029/JB095iB04p05101.

[12]   Heinson YW, Maughan JB, Heinson WR, Chakrabarti A, Sorensen CM. Light scattering Q-space analysis of irregularly shaped particles. Journal of Geophysical Research: Atmospheres 2016;121:682–91. https://doi.org/10.1002/2015JD024171.

[13]   Sorensen CM, Fischbach DJ. Patterns in Mie scattering. Optics Communications 2000;173:145–53. https://doi.org/10.1016/S0030-4018(99)00624-0.

[14]   Berg MJ, Sorensen CM, Chakrabarti A. Patterns in Mie scattering: evolution when normalized by the Rayleigh cross section. Appl Opt 2005;44:7487. https://doi.org/10.1364/AO.44.007487.

[15]   Sorensen C, Heinson Y, Heinson W, Maughan J, Chakrabarti A. Q-Space Analysis of the Light Scattering Phase Function of Particles with Any Shape. Atmosphere 2017;8:68. https://doi.org/10.3390/atmos8040068.

[16]   Longtin DR, Shettle EP, Hummel JR, Pryce JD. A Wind Dependent Desert Aerosol Model: Radiative Properties, Air Force Geophys. Lab., Air Force Syst. Command Hanscom Air Force Base, Mass, AFGL-TR-88-0112, 115, 1988.

[17]   Bedidi A, Cervelle B. Light scattering by spherical particles with hematite and goethitelike optical properties: Effect of water impregnation. J Geophys Res 1993;98:11941–52. https://doi.org/10.1029/93JB00188.

[18]   Wang Y, Chakrabarti A, Sorensen CM. A light-scattering study of the scattering matrix elements of Arizona Road Dust. Journal of Quantitative Spectroscopy and Radiative Transfer 2015;163:72–9. https://doi.org/10.1016/j.jqsrt.2015.05.002.

[19]   Ferri F. Use of a charge coupled device camera for low-angle elastic light scattering. Review of Scientific Instruments 1997;68:2265–74. https://doi.org/10.1063/1.1148135.

[20]   Ilavsky J, Zhang F, Andrews RN, Kuzmenko I, Jemian PR, Levine LE, et al. Development of combined microstructure and structure characterization facility for *in situ* and *operando* studies at the Advanced Photon Source. J Appl Crystallogr 2018;51:867–82. https://doi.org/10.1107/S160057671800643X.

[21]   Oh C, Sorensen CM. Scaling Approach for the Structure Factor of a Generalized System of Scatterers. Journal of Nanoparticle Research 1999;1:369–77. https://doi.org/10.1023/A:1010033111039.

[22]   Herrmann HJ. Geometrical cluster growth models and kinetic gelation. Physics Reports 1986;136:153–224. https://doi.org/10.1016/0370-1573(86)90047-5.

[23]   Jackson JD. Classical Electrodynamics, 3rd Edition. New York: Wiley; 1998.

[24] Querry MR. Optical constants of minerals and other minerals from the millimeter to the UV. Report CRDEC-CR-88009, US Army, Aberdeen, MD, 1987. n.d.

[25] Meland B, Kleiber PD, Grassian VH, Young MA. Visible light scattering study at 470, 550, and 660nm of components of mineral dust aerosol: Hematite and goethite. Journal of Quantitative Spectroscopy and Radiative Transfer 2011;112:1108–18. https://doi.org/10.1016/j.jqsrt.2010.12.002.

[26] A. Guinier, G. Fournet Small-angle scattering of X-rays Wiley, New York (1955) n.d.

[27] Sorensen CM, Shi D. Guinier analysis for homogeneous dielectric spheres of arbitrary size. Optics Communications 2000;178:31–6. https://doi.org/10.1016/S0030-4018(00)00601-5.

[28] Maughan JB, Sorensen CM. Application of the scaling approach to particles having simple, fundamental shapes, in the Rayleigh–Debye–Gans diffraction limit. Journal of Quantitative Spectroscopy and Radiative Transfer 2019;222–223:190–5. https://doi.org/10.1016/j.jqsrt.2018.10.037.

[29] Heinson WR, Chakrabarti A, Sorensen CM. Crossover from spherical particle Mie scattering to circular aperture diffraction. J Opt Soc Am A 2014;31:2362. https://doi.org/10.1364/JOSAA.31.002362.

[30] Wang G, Chakrabarti A, Sorensen CM. Effect of the imaginary part of the refractive index on light scattering by spheres. J Opt Soc Am A 2015;32:1231. https://doi.org/10.1364/JOSAA.32.001231.

[31] Shkuratov Y, Bondarenko S, Ovcharenko A, Pieters C, Hiroi T, Volten H, et al. Comparative studies of the reflectance and degree of linear polarization of particulate surfaces and independently scattering particles. Journal of Quantitative Spectroscopy and Radiative Transfer 2006;100:340–58. https://doi.org/10.1016/j.jqsrt.2005.11.050.

[32] Zubko E, Shkuratov Y, Mishchenko M, Videen G. Light scattering in a finite multi-particle system. Journal of Quantitative Spectroscopy and Radiative Transfer 2008;109:2195–206. https://doi.org/10.1016/j.jqsrt.2008.03.007.

[33] Lumme K, Penttilä A. Model of light scattering by dust particles in the solar system: Applications to cometary comae and planetary regoliths. Journal of Quantitative Spectroscopy and Radiative Transfer 2011;112:1658–70. https://doi.org/10.1016/j.jqsrt.2011.01.016.

[34] Tishkovets VP, Petrova EV, Mishchenko MI. Scattering of electromagnetic waves by ensembles of particles and discrete random media. Journal of Quantitative Spectroscopy and Radiative Transfer 2011;112:2095–127. https://doi.org/10.1016/j.jqsrt.2011.04.010.

[35] Petrova EV, Tishkovets VP. Light scattering by aggregates of varying porosity and the opposition phenomena observed in the low-albedo particulate media. Journal of Quantitative Spectroscopy and Radiative Transfer 2011;112:2226–33. https://doi.org/10.1016/j.jqsrt.2011.01.011.

[36] Mishchenko MI, Liu L, Mackowski DW, Cairns B, Videen G. Multiple scattering by random particulate media: exact 3D results. Opt Express 2007;15:2822. https://doi.org/10.1364/OE.15.002822.

[37] Mishchenko MI, Dlugach JM, Yurkin MA, Bi L, Cairns B, Liu L, et al. First-principles modeling of electromagnetic scattering by discrete and discretely heterogeneous random media. Physics Reports 2016;632:1–75. https://doi.org/10.1016/j.physrep.2016.04.002.

[38] Mackowski DW, Mishchenko MI. A multiple sphere T-matrix Fortran code for use on parallel computer clusters. Journal of Quantitative Spectroscopy and Radiative Transfer 2011;112:2182–92. https://doi.org/10.1016/j.jqsrt.2011.02.019.

[39] Mokhtari T, Sorensen CM, Chakrabarti A. Multiple-scattering effects on static light-scattering optical structure factor measurements. Appl Opt 2005;44:7858. https://doi.org/10.1364/AO.44.007858.